Check for updates

Advanced Functional Materials

ADVANCED FUNCTIONAL MATERIALS
www.afm-journal.de

RESEARCH ARTICLE OPEN ACCESS

Anomalous Pressure-Temperature Ultrahigh Sensitivities in Atomically Engineered Carbonitride MXenes for Multifunctional Wearable Human–Machine Interfaces: Joint Computational–Experimental Elucidations

Debananda Mohapatra[1,2,3] | Ju-Hyoung Han[3] | Hyun Jin Kang[4] | Jeong Eun Byun[4] | Seonghun Lee[1] | Sanghyuk Lee[5] | Yeseul Son[1] | Jaeeun Park[1] | Tae Joo Shin[1] | Youngho Kang[5] | Jung Woo Lee[4] | Soon-Yong Kwon[1,3] | Soo-Hyun Kim[1,3]

[1]Graduate School of Semiconductor Materials and Devices Engineering, Ulsan National Institute of Science and Technology (UNIST), Ulsan, Republic of Korea | [2]UNIST InnoCORE AI-Space Solar Initiative, Ulsan National Institute of Science and Technology (UNIST), Ulsan, Republic of Korea | [3]Department of Materials Science and Engineering, Ulsan National Institute of Science and Technology (UNIST), Ulsan, Republic of Korea | [4]Department of Materials Science and Engineering, Pusan National University, Busan, Republic of Korea | [5]Department of Materials Science and Engineering, Incheon National University, Incheon, Republic of Korea

Correspondence: Debananda Mohapatra (debanandam@unist.ac.kr) | Youngho Kang (youngho84@inu.ac.kr) | Jung Woo Lee (jungwoolee@pusan.ac.kr) | Soon-Yong Kwon (sykwon@unist.ac.kr) | Soo-Hyun Kim (soohyunsq@unist.ac.kr)

Received: 12 November 2025 | **Revised:** 10 March 2026 | **Accepted:** 24 March 2026

Keywords: anomalous sensitivities-responsiveness | atomically engineered carbonitride MXenes | first-principles calculations | human-machine interface | wearable-multifunctional sensors

ABSTRACT

In the era of autonomous systems and multifunctional devices, sensors serve as vital sensory components in our Internet of Things and technologically advanced society. At the end of the synthetic 2D nanomaterials research, MXenes are not just chemicals but materials, depending on how they are synthesized for targeted applications, such as dual-functional temperature and pressure-sensitive wearable sensing. The current findings introduce the potential strategic role of nitrogen atoms to the Ti-Carbonitride (Ti_3CNT_z) structure in a controlled compositional stoichiometry of $Ti_3C_{1.8}N_{0.2}T_z$, $Ti_3C_{1.5}N_{0.5}T_z$, Ti_3CNT_z, $Ti_3C_2T_x$ to deliver an ultrahigh sensitivity (300%–400% temperature & pressure sensitivity enhancement) and durability in real-time human-machine sensing interface applications. These recorded outstanding dual-sensing performance outplays many other MXene stoichiometries, graphene-related 2D nanomaterials, and their associated composites. Synchrotron radiation-based X-ray absorption fine structure and density functional theory analysis reveal that incorporating low N content (e.g., $Ti_3C_{1.8}N_{0.2}T_z$) enhances temperature sensitivity by boosting electrical conductivity, and an upshift in the vibrational spectrum with increased lattice deformability significantly improves pressure sensitivity. We provide valuable insights for developing advanced sensing materials, emphasizing the need to investigate the fundamental mechanisms that control the interactions among layered 2D MXene materials and the sensing device functions that bridge human and machine interfaces.

Debananda Mohapatra, Ju-Hyoung Han, Hyun Jin Kang, and Jeong Eun Byun contributed equally to this work.

This is an open access article under the terms of the Creative Commons Attribution License, which permits use, distribution and reproduction in any medium, provided the original work is properly cited.

© 2026 The Author(s). *Advanced Functional Materials* published by Wiley-VCH GmbH

1 | Introduction

The increasing demand for cutting-edge nanomaterials to optimize sensor functionality, especially in the realm of swift and precise detection sensors, has now become a pressing necessity. An uninterruptible sensing device's functionality is crucial to ensure the safety of personal healthcare gadgets. The efficacy of wearable pressure sensors in terms of sensing capability and long-term sensitivity retention is undeniably contingent upon the meticulous selection of sensing materials to function as active electrodes, their earth abundance, deposited substrates, and the overall geometric design [1–3]. Remarkably flexible and wearable pressure and temperature sensors are essential in diverse areas such as electronic skins, personal healthcare treatments, speech recognition, intelligent robots, and automobiles [4, 5]. Particularly in the case of piezoelectric pressure sensors, through their reliable piezoelectric effect, their exceptional ability allows them to convert physiological signals into electronic signals effectively [5, 6]. During the era before and after the COVID-19 pandemic, there has been a significant increase in the importance of temperature sensors and their immediate sensitivity, especially from the perspective of early medical diagnoses and personal healthcare. The selection and utilization of sensing materials and device structures are crucial in the realm of point-of-care diagnostics, as well as the development of commercial-grade wireless and wearable sensing devices. One state-of-the-art sensing earth-abundant electrode material that could deliver both temperature and pressure sensing performance, with durability, is the need of the hour.

Over recent years, the domain of 2D nanomaterials [7, 8], particularly the MXene family, has been emerging. These are transition metals based on carbide, nitride, or carbonitride, depending upon the presence of carbon, nitrogen, or both in their stoichiometric compositions [3, 9–11]. They are primarily derived from their parent MAX phase, which keeps the crystal structure intact. This ever-expanding 2D thriving MXene family has demonstrated promising sensing capabilities owing to their layered 2D geometry, expansive open surface area, electrical conductivity, tunability in surface functionalization, and electrochemical sensitivity combined with robust mechanical properties [10, 12]. Given their similarities to graphene in terms of microstructure and attributes, these 2D MXene nanomaterials have garnered significant attention from the research communities focusing on wearable sensing technologies for temperature and pressure, surpassing the interest in 1D nanowires/nanotubes, 2D dichalcogenides, nanosheets, nanoplatelets, metallic nanoparticles, and alloys. However, most of the MXene sensing research and exploration centers around the $Ti_3C_2T_x/Ti_2CT_x$ (Ti-MXene), though there are significant opportunities in carbonitride MXene, where the presence of nitrogen in the Ti_3CNT_z MXene structure would be a game changer. It is mainly their structural robustness, hydrophilicity, and ease of processing in solutions, while being highly electrically conductive, that gives an advantage to both TiC and TiN character in the Ti_3CNT_z MXene structure. Suppose more electronegative nitrogen atoms are introduced to the Ti-MXene structure; the possibility of electron density throughout the carbonitride MXene structure drastically changes [13]. Nitride-based MXenes have been less explored than carbide-based MXenes due to their inherent instability, including susceptibility to dissolution and oxidation, and their reported properties have generally been inferior [14]. A particular case would be an appropriate balance of nitrogen and carbon atoms in carbonitride MXene. The intrinsic microstructure of 1D nanowires/nanotubes and 2D graphene (high compressive modules, ≈1 TPa) cannot be easily atomically manipulated to enhance the sensitivity of the pressure sensor, as achieving high sensitivities necessitates significant deformation of their microstructures [5, 15]. It is due to their internal atomic structure that restricts any movement under external stimuli. Meanwhile, the novel Ti-carbonitride MXene with a widened interlayer structure associated with an accordion-like open internal microstructure readily undergoes more mechanical flexibility than conventionally used CNTs and graphene. Notably, the demand for high-pressure sensitivities calls for substantial structural deformation under conditions of minimal strain, where achieving high flexibility necessitates strongly interconnected Ti-Carbonitride MXene networks of active materials at larger strains.

A careful selection and purity of carbonitride MAX phases and their carbonitride MXene synthesis approaches are crucial for stable sensing device function. The MXene literature also lacks thorough research on the purity of the carbonitride MAX phase [16–18]. Hence, developing an appropriate synthesis condition and high-quality parent carbonitride MAX phases to be focused on having commercial-grade wireless and wearable sensing devices. Commercially available carbonitride MAX powders/phases contain significant levels of impurities and secondary phases, with non-stoichiometric compositions and reduced purity [16–18]. When the parent MAX phase is not as pure as desired for its MXene phase, it will result in targeted applications and their devices' durability, e.g., wearable sensing devices. Existing impurities could also result in uneven carbonitride MXene flakes stacking electrical conductivity, malfunctioning any sensing applications in the real world. Therefore, to significantly deliver high sensitivity in a portable sensing device, it is of utmost importance to ensure the high-quality parent carbonitride MAX phases that are lacking in ever-expanding 2D MXene families and existing literature to date. $Ti_3C_2T_x$ titanium MXene could also be thought of as isostructural with titanium carbonitride, Ti_3CNT_z, where 50% of carbon atoms are replaced by nitrogen atoms, leading to drastic manipulation in electronic properties.

Further manipulation of nitrogen atoms to the carbonitride structure could also lead to additional Ti-N hybridization, contributing to the additional density of states near the Fermi level [13, 19, 20]. This hybridization also plays a crucial role in facilitating the Ti 3d unoccupied states toward further nitrogen atom incorporation. Therefore, it would be fascinating to investigate the true role of nitrogen atoms in Ti-Carbonitride for practical wearable sensing devices at the human-machine interface. Detailed density function theory (DFT) calculations are dedicated to understanding nitrogen's role in sensing device performances, which remained unexplored in the MXene field both computationally and experimentally. Also, these exceptional contributions aimed at designing dual wearable sensing device applications, such as temperature and pressure practical sensors at the human-machine interface. The strategic introduction

16163028, 0, Downloaded from https://advanced.onlinelibrary.wiley.com/doi/10.1002/adfm.202530479 by Ulsan National Institute Of, Wiley Online Library on [09/04/2026]. See the Terms and Conditions (https://onlinelibrary.wiley.com/terms-and-conditions) on Wiley Online Library for rules of use; OA articles are governed by the applicable Creative Commons License

of nitrogen atoms in the Ti-Carbonitride compositional stoichiometries, influencing wearable pressure and temperature sensing mechanisms, performance parameters are precisely investigated using DFT-based computational techniques, advanced synchrotron radiation-based X-ray absorption fine structure (XAFS) on both near edge structure (XANES), extended X-ray absorptions (EXAFS), Wavelet-transformed EXAFS (WT-EXAFS), and Fourier-transformed EXAFS (FT-EXAFS) tools.

2 | Results and Discussions

2.1 | Advanced Synchrotron Radiation Spectroscopic Evidence on Ti-Carbonitride and Engineered Ti-Carbonitride MXenes

The targeted etching of $Ti_3AlC_{2-x}N_x$ (x = 0, 0.2, 0.5, and 1) carbonitride MAX phases to generate $Ti_3C_{2-x}N_xT_z$ (x = 0, 0.2, 0.5, and 1) carbonitride MXenes provides a means to engineer the interlayer spacing, internal layered microstructure, surface functional groups, and crystal structure. These are all fundamental elements that mainly depend on the purity and the quality of parent MAX phases, which influence the characteristics of carbonitride MXenes in various applications. Given the synthesis technique and preparation processes, which decisively affect the quality of the carbonitride MXene phase, we comprehensively investigated the purity of their parent MAX phase.

The XRD patterns of $Ti_3AlC_{2-x}N_x$ (x = 0, 0.2, 0.5, and 1) indicate well-defined crystal structures without the presence of intermediate species or secondary phases. Silicon was used to calibrate the peak shifts caused by nitrogen substitution (Figure S1A). An enlarged view of the XRD patterns for the (002) and (105) planes reveals peak shifts from $2\theta \approx 9.5°$ to 9.6° and 41.6° to 42.1°, respectively, which indicates a contraction of the unit cell volume due to successful nitrogen incorporation (Figure S1B). This lattice shrinkage might result from replacing carbon atoms with smaller nitrogen atoms [21–23]. The higher electronegativity of nitrogen than carbon could lead to the unit cell volume contraction, causing the shifting of the prominent (002) and (105) peaks. Figure S1C demonstrates the successful synthesis of multi-layered MXene ($Ti_3C_{2-x}N_xT_z$). The peak located at $2\theta \approx 9.5°$, corresponding to the (002) plane of the MAX phase, diminished, while a new peak emerged, corresponding to the (002) plane of the MXene phase. As x increased from 0 to 1, this (002) peak shifted to a lower 2θ, indicating an expanded d(002) from 12.58 Å to 13.59 Å. The observed differences in the FWHM of the MXene (002) peak are attributed to variations in the drying conditions during film preparation, which can influence the nanosheets' 2D stacking order and interlayer swelling [23–25].

Laboratory-processed high-quality parent carbonitride MAX phases ($Ti_3AlC_{2-x}N_x$) used for producing $Ti_3C_2T_x$, Ti_3CNT_z, and other atomic nitrogen-incorporated engineered carbonitride MXene materials, $Ti_3C_{1.5}N_{0.5}T_z$, and $Ti_3C_{1.8}N_{0.2}T_z$. Figure S2 shows the evaluated electrical conductivity of annealed $Ti_3C_2T_x$, $Ti_3C_{1.8}N_{0.2}T_z$, $Ti_3C_{1.5}N_{0.5}T_z$, and Ti_3CNT_z MXene films. All samples were thermally annealed at 250°C for 2 h to remove the confined intercalant molecules/ions in a vacuum oven prior to electrical measurement. Electrical conductivity was evaluated using a four-point probe method. Pristine $Ti_3C_2T_x$ exhibited a conductivity of 21,197 S/cm, while $Ti_3C_{1.8}N_{0.2}T_z$ showed the highest value of 22,727 S/cm, indicating that a small degree of nitrogen substitution can enhance electronic transport, facilitating enhanced sensing durability. However, conductivity decreased significantly as the nitrogen content increased, demonstrating the substantial influence of atomic nitrogens and their stochiometry on Ti_3CNT_z MXene. $Ti_3C_{1.5}N_{0.5}T_z$ and Ti_3CNT_z displayed reduced conductivities of 13,584 S/cm and 7,143 S/cm, respectively, suggesting that excessive nitrogen incorporation may induce interlayer defects, stacking, and charge scattering phenomena within the MXene lattice. It can be observed that in Figure 1A, Al is reduced, and Ti is oxidized in all samples, as indicated by the increase in the absorption edge energy in XANES. Considering the MXene structure, the peak at approximately 1.5 Å in the FT-EXAFS results in Figure 1B can also be attributed to Ti—C or Ti—N bonds, while the peak at around 2.5 Å corresponds to Ti-Ti bonds. Since the intensity of the peaks in EXAFS is primarily related to the coordination number, a higher coordination number is strongly reflected in the intensity of the peaks. In addition to this, the factors that influence the peak's intensity are possibly related to the few disorders associated with the crystallinity of the synthesized carbonitride parent MAX and MXene crystal structures. Therefore, the peak may come out lower if there is disorder in the crystal structure.

When comparing the relative intensity of the Ti—C/N peak mentioned earlier in FT-EXAFS, it is observed to be strongest in the $Ti_3C_{1.8}N_{0.2}T_z$ sample, showing a tendency to decrease as the amount of nitrogen doping increases. Similarly, this trend can also be observed in the Ti—Ti bonding, where it is most pronounced in the $Ti_3C_{1.8}N_{0.2}T_z$ sample and gradually decreases. When looking at the trends of the two peaks, it is expected that the sensing performance improvement can be explained differently. Previously, suppose we aimed to explain the changes in electrical conductivity (Figure S2) based on the coordination number of Ti-N bonds due to nitrogen incorporation, as mentioned earlier. In that case, it seems we can now explain that the improvement in crystallinity resulting from the reduction of disorder with significantly enhanced electrical conductivity leads to changes in dual sensing performance.

Moreover, to enhance the visibility of the above content, we compared the results using WT-EXAFS in Figure 1C. In general, it is explained that in EXAFS, atomic number (Z) differentiation is possible when there is a difference of 3 or more in atomic numbers. For this reason, accurately distinguishing between C and N is fundamentally challenging. Therefore, WT-EXAFS was employed to represent them differently. In the given results, the X-axis represents the wavevector ($Å^{-1}$), the Y-axis represents the bond length (Å), and the contrast refers to the peak amplitude. First of all, the peak at 1.5 Å in R-space indicates a Ti—C/N bond, similar to FT-EXAFS. In the $Ti_3C_2T_x$ specimen without nitrogen doping, the maximum occurs at about 2.85 $Å^{-1}$, while in the $Ti_3C_{1.8}N_{0.2}T_z$ sample, the maximum appears at a slightly larger value of 3.45 $Å^{-1}$. In WT-EXAFS, when the atomic number is small, peaks appear at low k ($Å^{-1}$), while, conversely, for larger atomic numbers, peaks appear at high

16163028, 0, Downloaded from https://advanced.onlinelibrary.wiley.com/doi/10.1002/adfm.202530479 by Ulsan National Institute Of, Wiley Online Library on [09/04/2026]. See the Terms and Conditions (https://onlinelibrary.wiley.com/terms-and-conditions) on Wiley Online Library for rules of use; OA articles are governed by the applicable Creative Commons License

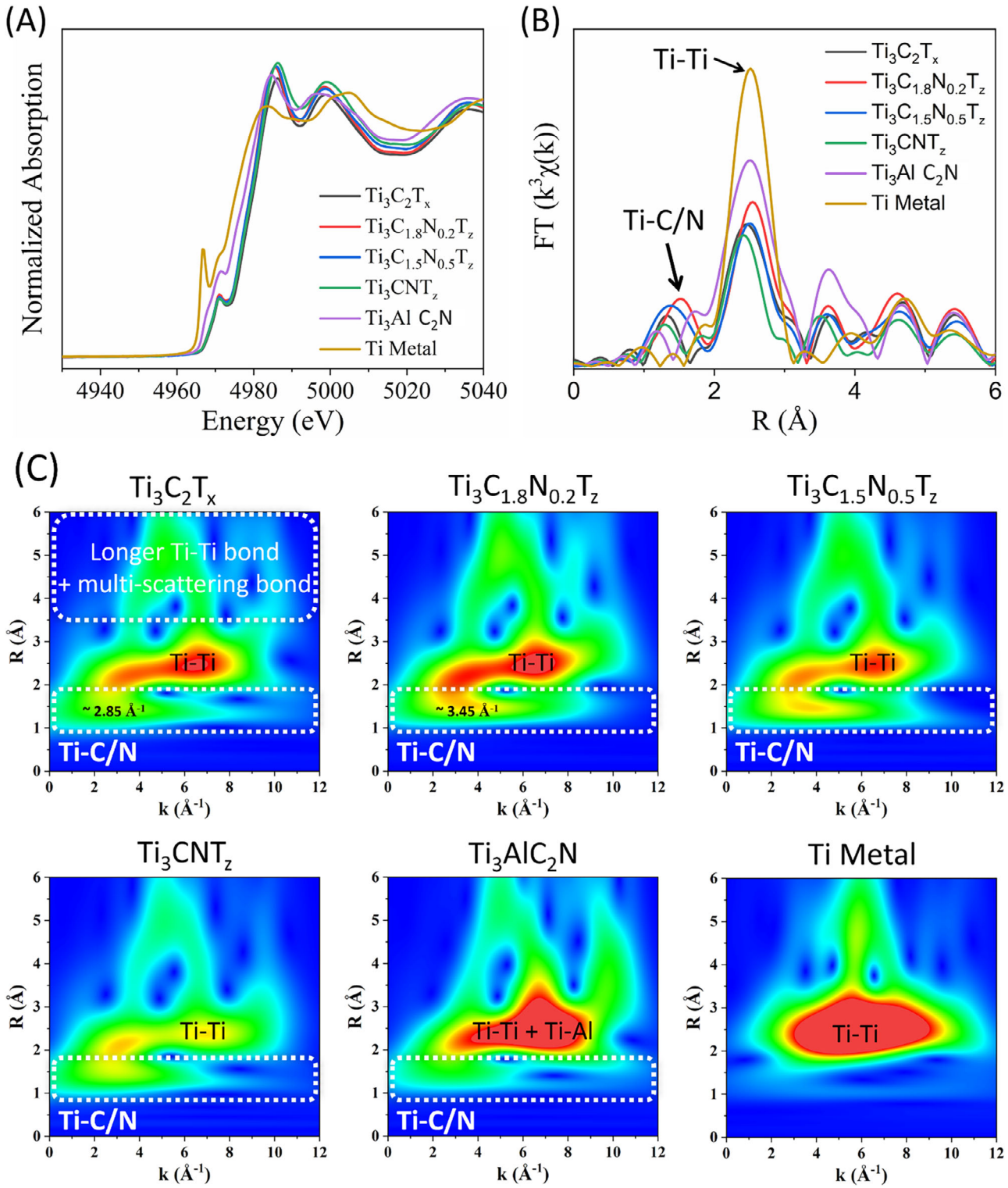

FIGURE 1 | Advanced synchrotron radiation X-ray absorption fine structure (XAFS) chemical bonding evidence on the role of nitrogen in engineered Ti_3CNT_z carbonitrides MXene for dual pressure and temperature sensitivity, (A) X-ray absorption near edge structure (XANES), (B) Fourier-transformed extended (FT-EXAFS), and (C) Wavelet-transformed EXAFS (WT-EXAFS) and Fourier-transformed EXAFS (FT-EXAFS).

k ($Å^{-1}$). Therefore, although the difference is not significant, the wavevector appearing at about 0.6 $Å^{-1}$ is thought to be due to the presence of nitrogen around titanium. As N atoms are incorporated in MXenes, a peak emerges in the R (1–2) Å region (white bottom rectangles in Figure 1C). This peak reaches its maximum intensity in the $Ti_3C_{1.8}N_{0.2}T_z$ (x = 0.2) sample, exhibiting optimized structural and highest electrical properties (electrical conductivity, ~22,700 S/cm)and remarkably high sensing performances discussed below. However, for $Ti_3C_{1.5}N_{0.5}T_z$ (x = 0.5) and Ti_3CNT_z (x = 1), the peak intensity decreases due

16163028, 0, Downloaded from https://advanced.onlinelibrary.wiley.com/doi/10.1002/adfm.202530479 by Ulsan National Institute Of, Wiley Online Library on [09/04/2026]. See the Terms and Conditions (https://onlinelibrary.wiley.com/terms-and-conditions) on Wiley Online Library for rules of use; OA articles are governed by the applicable Creative Commons License

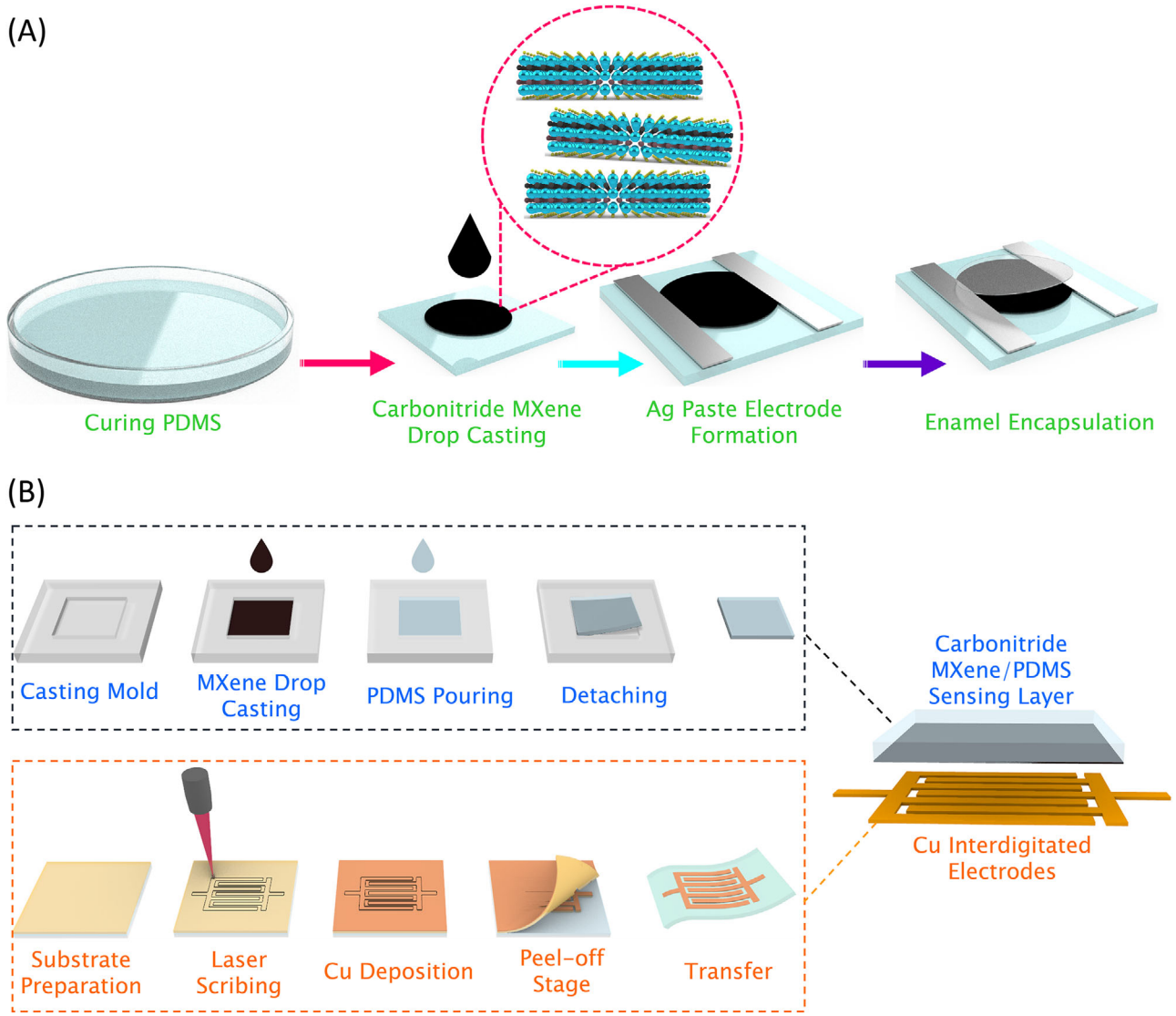

SCHEME 1 | Introducing Ti-Carbonitride (Ti_3CNT_z) and engineered Ti-Carbonitride MXenes for real-time skin temperature, respiration, proximity thermography, and flexible pressure sensing to vital human motions and a range of physiological activities at the human-machine interface. (A) Temperature and (B) Pressure sensor fabrication processes.

to the deterioration of the intrinsic properties of the MAX phase caused by the additional/sufficient incorporation of N atoms.

2.2 | Sensitivity and Sensing Performances of Engineered Ti-Carbonitride MXenes-Based Temperature Sensor

Figure S2 shows the temperature sensitivity of $Ti_3C_2T_x$, $Ti_3C_{1.5}N_{0.5}T_z$, Ti_3CNT_z, and $Ti_3C_{1.8}N_{0.2}T_z$, which have different N and C stoichiometries. The overall atomic structure of each material is shown in Scheme 1A and supplementary text (see Materials and Methods), and the temperature sensors were fabricated by drop-casting MXene powder onto PDMS (Scheme 1A). When the temperature performance was measured using an MXene film, the resistance was extremely low, ranging from approximately 10 to 100 Ω, making it challenging to observe resistance changes with temperature. However, temperature-dependent resistance variations were clearly observed when using a powder-based sample. This phenomenon is presumed to originate from band structure modifications induced by carbonitride MXene material density changes upon incorporating nitrogen atoms. As the material transitions from a film to a powder, the atomic density decreases, leading to the band gap opening phenomenon [26]. During the fabrication process, the MXene materials were encapsulated to ensure the stability of the temperature sensors. As shown in Figures S3A,B, when the temperature was increased in 5°C increments within the range of 25–35°C, the resistance of the unencapsulated sensor tended to decrease continuously, even at the same temperature. In contrast, the encapsulated sensor maintained relatively stable resistance. Figure S3C presents the resistance response at 30°C, indicating that the encapsulated sample improved the stability by approximately 15%, leading to enhanced performance.

The sensitivity of the fabricated flexible temperature sensor was measured within the skin temperature range (25–40°C).

16163028, 0, Downloaded from https://advanced.onlinelibrary.wiley.com/doi/10.1002/adfm.202530479 by Ulsan National Institute Of, Wiley Online Library on [09/04/2026]. See the Terms and Conditions (https://onlinelibrary.wiley.com/terms-and-conditions) on Wiley Online Library for rules of use; OA articles are governed by the applicable Creative Commons License

The resistance response (%) was calculated to determine the sensitivity, and it is defined as follows:

$$Resistance\ response\ \ (\%) = \frac{R - R_0}{R_0} \times 100\ \ (\%) \qquad (1)$$

where R denotes the resistance measured in real-time at the altered temperature, and R_0 represents the resistance at the reference temperature. Additionally, the equation for sensitivity is as follows:

$$Sensitivity\ \ \left[\%\ C^{-1}\right] = \frac{R - R_0}{R_0 \Delta T} \times 100\ \ (\%) \qquad (2)$$

where ΔT is the temperature variation and $\Delta R = R - R_0$.

Based on this equation, the sensitivities of $Ti_3C_2T_x$, $Ti_3C_{1.5}N_{0.5}T_z$, Ti_3CNT_z and $Ti_3C_{1.8}N_{0.2}T_z$ were 5.5% °C^{-1}, 4.5% °C^{-1}, 6.4% °C^{-1}, and 15.9% °C^{-1}, respectively. Among the four samples in Figures S4A-D, $Ti_3C_{1.8}N_{0.2}T_z$ exhibited the highest sensitivity and excellent linearity. As described in previous theoretical studies and DFT calculations [20, 27, 28], atomic nitrogen incorporations modify the electronic structure, leading to a high resistance change rate due to the low initial resistance. Determining the optimal nitrogen doping concentration is essential for temperature sensitivity. According to Mattiessen's rule, the total scattering probability can be described as the sum of contributions from lattice vibrations and impurity scattering based on probability theory. Excessive doping can lead to an increase in impurity scattering, which does not scale proportionally with temperature, thereby diminishing the effect of temperature on resistance. Therefore, it is crucial to strike a balance between electrical conductivity and electron scattering [29]. In this study, we identified $Ti_3C_{1.8}N_{0.2}T_z$ as the optimal atomic nitrogen incorporated carbonitride MXene stochiometry, where the material exhibits low initial conductivity while minimizing temperature-independent scattering.

Furthermore, as shown in Table S1, the $Ti_3C_{1.8}N_{0.2}T_z$ temperature sensor exhibited an exceptionally high sensitivity of 15.9% °C^{-1}, significantly exceeding that of previously reported wearable temperature sensors fabricated from the MXene and also their various composites with graphene, CNT, polymers and atomic layer deposited (ALD) precious metals, such as ALD-Ru, ALD-Ir [3, 11]. Figures S4E,F present the sensing performance of the $Ti_3C_{1.8}N_{0.2}T_z$ temperature sensor, which demonstrates the highest sensitivity. Figure S4E shows the reversibility by cooling it from 40°C and then heating it back to 25°C. During this process, the resistance values exhibited an almost identical trend at the same temperatures. However, the linearity decreased significantly, possibly due to the electron scattering events compared to when only the heating process was performed, suggesting the need for further research and improvement in this novel concept of atomic nitrogen-engineered carbonitride MXene. Figure S4F shows the sensor's response when warm and cold water drops were applied at approximately 30°C. The warm water elicited a response within 20 s, while the cold water required around 30 s. These results demonstrate that the fabricated temperature sensor can detect temperature changes within a matter of seconds.

2.3 | Sensitivity and Sensing Performances of Engineered Ti-Carbonitride MXenes-Based Flexible Pressure Sensor

The whole fabrication process of the Ti-Carbonitride MXene/PDMS-based flexible pressure sensor is depicted in Scheme 1B and supplementary text (see materials and methods). A facile laser process was employed to fabricate copper electrodes in the form of interdigitated electrodes, which were then transferred to a silicon substrate. The MXene-based composite sensing layer was prepared by drop-casting MXene solution into a mold with an area of 1 cm^2. PDMS was subsequently poured onto the MXene, allowing it to penetrate between the powders and naturally form a composite sensing layer composed of a PDMS insulating matrix and MXene conductive filler. The Ti-Carbonitride MXene powders were densely embedded by simple and economical mold-based fabrication within the PDMS, maintaining physical stability even in bending or compression. Figure S5 shows a cross-sectional SEM image of the composite sensing layer, where Ti-Carbonitride is stably embedded in the PDMS at a high density with an average thickness of approximately 50 μm. EDS elemental mapping further proved the detailed composition, as shown in Figure S6. The Si and O elements originating from the PDMS and the uniformly dispersed major Ti elements from the Ti-Carbonitride MXene sheets indicate a well-distributed Ti-Carbonitride filler within the PDMS matrix. PDMS was also used as a protective layer to prevent MXene oxidation and reduce the influence of ambient humidity on sensor performance [30–32]. Finally, the top and bottom layers were combined, indicating mechanical flexibility as shown by lightly mounting onto a finger in Figure S7.

The Ti-Carbonitride MXene pressure sensor functions by using the piezoresistive effect induced by changes in the density of conductive fillers. When no pressure is applied, the conductive Ti-Carbonitride MXene fillers are relatively separated, allowing only a small amount of current to flow through limited percolation paths. At this stage, the resistivity of the composite sensing layer is high due to the insulating nature of the polymer matrix [30]. When pressure is applied, the distance between conductive MXene fillers in the PDMS decreases, bringing a dense electron transport path. This compression could enhance the formation of conductive pathways, significantly decreasing resistance and increasing current flow as high MXene filler density. Based on this percolation theory, the mechanism with the resistance change of the sensing layer is influenced by the distance between conductive fillers under applied pressure [30]. Furthermore, at the higher applied pressures, the tunneling effect can occur in the intra-flakes of Ti-Carbonitride MXene, enabling electrons to flow through the nanolayers as the interlayer distance is progressively reduced [31–34]. As the distance between MXene layers decreases upon pressure, each sheet begins to close and overlap, forming tunnel junctions [32–34]. This combined effect of percolation and potential tunneling contributes to the sensor's enhanced response to pressure, demonstrating the composite's effective piezoresistive properties.

The Ti-Carbonitride-based piezoresistive sensor's sensing properties were evaluated using a current measurement system at a constant voltage under different applied pressures. Figure 2A

16163028, 0, Downloaded from https://advanced.onlinelibrary.wiley.com/doi/10.1002/adfm.202530479 by Ulsan National Institute Of, Wiley Online Library on [09/04/2026]. See the Terms and Conditions (https://onlinelibrary.wiley.com/terms-and-conditions) on Wiley Online Library for rules of use; OA articles are governed by the applicable Creative Commons License

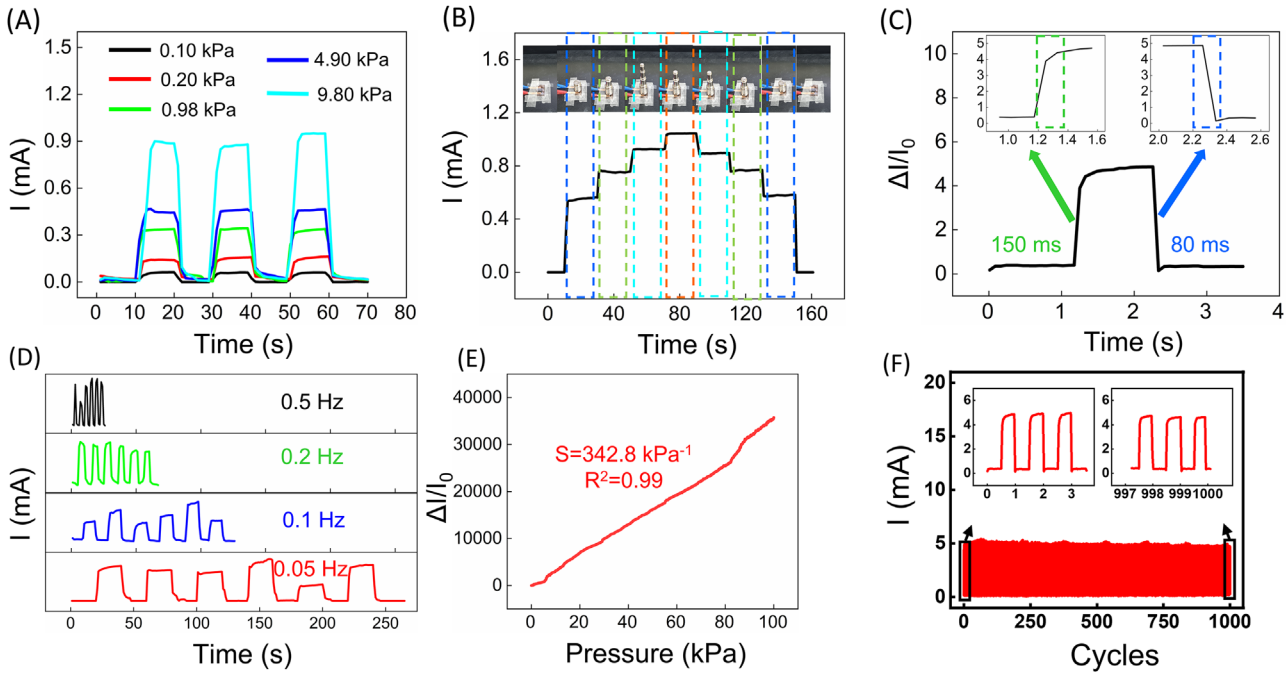

FIGURE 2 | Real-time pressure sensing properties and long-term performances of engineered Ti-Carbonitride MXene ($Ti_3C_{1.5}N_{0.5}T_z$). (A) The I-T characteristic curves of the fabricated sensor devices under the different pressures, (B) Sensing current response of the sensor devices from step pressure, (C) Responsivity and recovery time, (D) The frequency response performance of the sensors under 4.90 kPa, (E) Sensitivity under the applied pressure of 0 to 100 kPa, and (F) Stability and durability of the pressure sensor device ($Ti_3C_{1.5}N_{0.5}T_z$ MXene on PDMS surface) for 1000 loading-unloading cycles with a pressure loading of 20 kPa without any significant performance fading.

shows the current change at a constant voltage according to repeated pressure in the 100 Pa – 9.8 kPa range. The fast current on/off response represents reliability for detecting the various pressure levels. As shown in Figure 2B, the pressure sensor exhibits consistent and stable current changes when pressure is applied and removed stepwise using balance weights. It maintained reliable sensing performance without any degradation under reversible pressure variations. Especially in practical applications with high-speed operating conditions, short response and recovery times are essential for the sensor to detect rapid signals effectively. Figure 2C exhibits a rapid response and recovery time of 150 and 80 ms under 20 kPa, ensuring real-time monitoring of physiological or physical activity. Furthermore, the device presents a stable and uniform response to frequency changes controlled by loading time in Figure 2D. The result suggests that the pressure sensor tested at various frequencies exhibits excellent durability across a wide range of speed operating conditions. As well known, sensitivity is a sensing coefficient, representing the most critical indices for pressure sensors. Here, the pressure sensitivity (S) is defined as $S = (\Delta I/I_o)/\Delta P$, where I_o is the current without pressure, ΔI is the variation of the current under the applied pressure, and ΔP is the change of the applied pressure [35]. Figure 2E shows the change in the ratio of current ($\Delta I/I_o$) as a function of the applied pressure. The sensor composed of $Ti_3C_{1.5}N_{0.5}T_z$ MXene/PDMS has a high sensitivity of 342.8 kPa^{-1} and excellent linearity ($R^2 = 0.99$) within a range of 100 kPa. For comparison, the sensitivity of other Ti-Carbonitride MXenes was also measured (Figure S8), showing that the sensitivities of $Ti_3C_{1.5}N_{0.5}T_z$ (342.8 kPa^{-1}) and $Ti_3C_{1.8}N_{0.2}T_z$ (314.2 kPa^{-1}) are much higher than that of Ti_3CNT_z MXenes, which has a value of 68.4 kPa^{-1}. Higher conductivity enhances both electron tunneling and the percolation effect, optimizing charge transport efficiency [36–38]. In our case, well-controlled atomic nitrogen incorporation to the carbonitride MXene structure potentially engineers the electrical conductivity of those nitrogen-sufficient/deficient MXene samples from moderate to extremely high values (Figure S2), suggesting the semiconductor-to-metal transformation. The contact resistance between MXene sheets also responds sensitively to applied pressure, further contributing to the sensor's performance and corroborating the potential role of incorporated atomic nitrogens in the carbonitride MXene structure. This high sensitivity within a wide pressure range highlights its superior pressure-sensing abilities compared to sensors with various sensing materials and structures, as shown in Table S2.

The exceptional pressure sensitivity observed in $Ti_3C_{1.5}N_{0.5}T_z$ and $Ti_3C_{1.8}N_{0.2}T_z$ MXene can be fundamentally attributed to the optimized electronic structure induced by controlled nitrogen incorporation, as supported by electron-phonon scattering and lattice deformation DFT calculations in Section 2.4. Consequently, the sensing mechanism driven by the tunneling current between the Ti-Carbonitride MXene filler, combined with enhanced charge transport efficiency and minimized electron scattering, synergistically contributes to the ultrahigh sensitivity and durability of the pressure sensor [30, 39]. This ultrahigh sensitivity and strong linear relationship make Ti-Carbonitride a promising candidate for next-generation smart sensing applications. To further evaluate the pressure sensor's limit of detection, low-pressure sensing tests were performed using 0.3 g plastic beads. As shown in Figure S9A, the sensor exhibits clear current responses during loading and unloading under pressure, indicating a detection limit of

16163028, 0, Downloaded from https://advanced.onlinelibrary.wiley.com/doi/10.1002/adfm.202530479 by Ulsan National Institute Of, Wiley Online Library on [09/04/2026]. See the Terms and Conditions (https://onlinelibrary.wiley.com/terms-and-conditions) on Wiley Online Library for rules of use; OA articles are governed by the applicable Creative Commons License

approximately 30 Pa, whereas a stable increase in resistance is observed even with a small temperature change of 0.5°C (Figure S9B). Also, the long-term stability of the Ti-Carbonitride MXene sensing layer is crucial for the whole sensor device. To evaluate the durability of the sensing layer, a repeated loading/unloading test was conducted, comparing two fabrication methods: one with a coated MXene layer on the PDMS surface and the other with an MXene-embedded PDMS structure (Figure 2F; Figure S9C). In the sensor with a surface-coated layer, the current continuously decreased due to the detachment of the MXene powder from the substrate under dynamic stress, as shown in Figure S9C. In contrast, the composite sensing layer exhibited consistent and reproducible current signal responses to pressure during 1000 cycles without any significant degradation in Figure 2F. The MXene surrounded by PDMS maintained its intrinsic conductive layer with no destruction from mechanical stress, demonstrating the excellent stability of the pressure sensor.

2.4 | First-Principles Computational Analysis on the Impact of Nitrogen on Sensing Performance of Ti-Carbonitride MXene

To elucidate the impact of nitrogen (N) incorporation on the sensing performance of Ti-Carbonitride MXene, we performed density functional theory (DFT) calculations (see atomic models in Figure 3A). As the N content increases, the unit cell volume and interatomic distances of Ti—Ti and Ti—C/N bonds are slightly reduced, consistent with the synchrotron radiation-based FT-EXAFS analysis above. We examine how the electronic structure evolves with an increase in the amount of nitrogen that substitutes carbon in MXene. In Figure 3B (upper panel), we see that Ti-carbide MXene ($Ti_3C_2T_x$) has no band gap, confirming the metallic nature of the MXene material, corroborating experimentally evaluated electrical conductivity of ~21,200 S/cm. The analysis of the orbital-resolved local density of states (LDOS) reveals that Ti 3d states predominantly contribute to the electronic states near the Fermi level (E_F), while C and N 2p states provide smaller contributions (Figure S10). One of the main effects of nitrogen incorporation into Ti-carbide MXene is the upward shift of the E_F, which can be attributed to nitrogen having one more valence electron than carbon. The band structures exhibit only slight changes upon N incorporation, as shown in Figure S11. Notably, when the nitrogen concentration is low ($Ti_3C_{1.75}N_{0.25}T_z$), the density of states (DOS) near the E_F increases only slightly. This suggests that the increase in the E_F due to nitrogen incorporation leads to a rise in the kinetic energy (i.e., speed) of electron carriers near the E_F, which dominantly contributes to the electrical conductivity without a significant increase in the scattering rate. As a result, electrical conductivity improves with the slight nitrogen incorporation in this case. This trend is expected to be applicable to MXenes with experimentally relevant compositions (e.g., $Ti_3C_{1.8}N_{0.2}T_z$), which could not be explicitly simulated due to the finite supercell size, given the similar C:N ratio to the simulated $Ti_3C_{1.75}N_{0.25}T_z$ system. On the other hand, when the nitrogen concentration is too high ($Ti_3C_1N_1T_z$), the E_F shifts further into a region with a significantly higher density of states (DOS). As a result, conducting electrons experience more electron-phonon scattering due to the increased availability of empty states into which they can scatter [40]. Additionally, among the Ti 3*d* states, the $3d_{z^2}$ orbitals, which form ineffective conducting channels in layered MXenes due to inefficient orbital hybridization, predominantly contribute to the electronic states near the Fermi level (Figure S12). This observation indicates that the contribution of additional carriers introduced by excessive N doping to the overall conductivity is limited. Consequently, electrical conductivity is suppressed in N-rich samples due to increased carrier scattering, as confirmed by our experimental measurements shown in Figure S2.

Our computational results explain why low nitrogen content (i.e., $Ti_3C_{1.8}N_{0.2}T_z$ in experiments) is particularly advantageous for temperature sensitivity. As discussed earlier, the primary effect of low nitrogen (deficient-nitrogen) doping to Ti-carbide MXene, forming $Ti_3C_{1.8}N_{0.2}T_z$, is the substantial enhancement of electrical conductivity (~22,727 S/cm) as compared to the high nitrogen incorporation (sufficient-nitrogen), $Ti_3C_{1.5}N_{0.5}T_z$ (~13,584 S/cm), and $Ti_3C_1N_1T_z$ (~7,143 S/cm). This increase in the electrical conductivity corresponds to a reduction in the reference resistance (R_0 in Equation 2). As a result, the temperature sensitivity is significantly boosted, even if the temperature-dependent resistivity modulation (ΔR) does not grow significantly. On the other hand, further nitrogen incorporation, forming $Ti_3C_{1.5}N_{0.5}T_z$ and $Ti_3C_1N_1T_z$, enhances electron-phonon scattering due to the increased DOS near the E_F, leading to a stronger temperature dependence of ΔR. However, this also results in a higher reference resistivity simultaneously. Accordingly, these two opposing effects cancel each other out, preventing Ti-Carbonitride MXene with high nitrogen content from achieving greater temperature sensitivity (Figure S4).

On the other hand, pressure sensing measures current amplification, i.e., the conductivity enhancement of the sensor under applied pressure. As mentioned above, the piezoresistive effect, which refers to a decrease in the contact resistance between carbonitride MXene layers, plays a crucial role. Additionally, phonon hardening caused by pressure-induced compressive strain (ε) can be an intrinsic factor contributing to the pressure sensitivity of the carbonitride MXene sensor. For example, the phonon DOS of $Ti_3C_{1.75}N_{0.25}T_z$ shifts to higher frequencies when applying a compressive strain, as shown in Figure 3C. Upward shifts in phonon frequencies due to compressive strain are generally observed regardless of the composition. This phonon hardening results in less activation of vibrational modes at a given temperature, reducing electron-phonon scattering [41]. As a result, electrical conductivity increases when pressure is exerted. Incorporating nitrogen can enhance this effect by making the lattice more susceptible to deformation (Figure 3D); the energy increase due to lattice deformation is lower in $Ti_3C_1N_1T_z$ than in $Ti_3C_2T_x$. This arises from the fact that antibonding states between Ti and C near the E_F become more occupied due to the increase in electron density with increasing N content, thereby weakening the Ti-C bond [42]. However, excessive nitrogen incorporation negatively impacts pressure sensitivity due to changes in the electronic structure; smaller interatomic distances in the strained MXenes enhance the interactions between atomic orbitals, leading to a larger energy overlap between the higher Ti $3d_z$ and the lower 3*d* states (Figures S11 and S12). As a result, as shown in Figure 3B (lower panel), the DOS near the Fermi level in N-rich $Ti_3C_1N_1T_z$ increases significantly when a compressive strain is applied. This leads to enhanced electron-phonon scattering, which counteracts the conductivity improvement, ultimately

16163028, 0, Downloaded from https://advanced.onlinelibrary.wiley.com/doi/10.1002/adfm.202530479 by Ulsan National Institute Of, Wiley Online Library on [09/04/2026]. See the Terms and Conditions (https://onlinelibrary.wiley.com/terms-and-conditions) on Wiley Online Library for rules of use; OA articles are governed by the applicable Creative Commons License

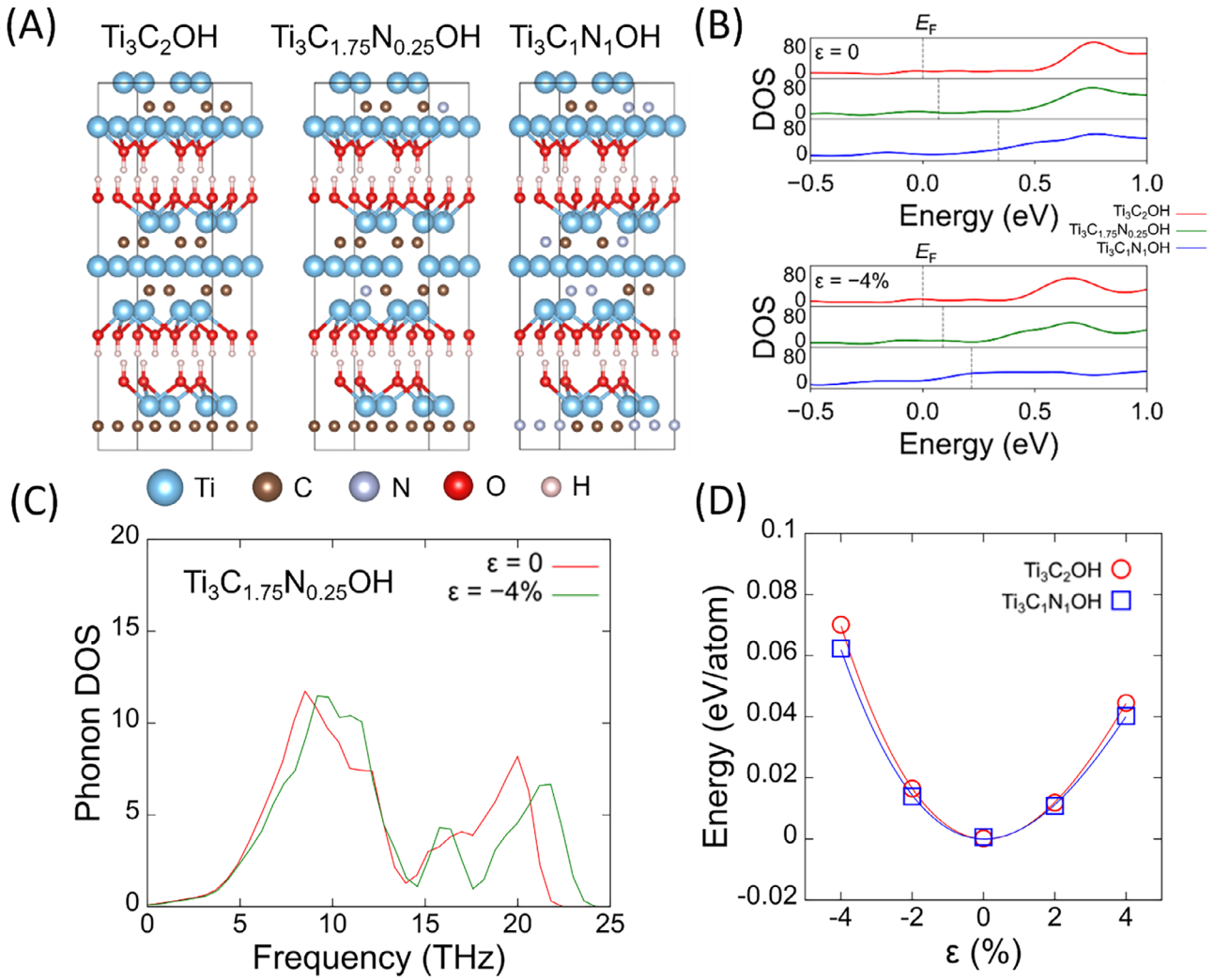

FIGURE 3 | (A) Atomic models of Ti-Carbonitride MXene. (B) Electronic density of states (DOS) of MXene depending on N content. Negative(positive) ε represents the compressive(tensile) strain. (C) Phonon DOS for $Ti_3C_{1.75}N_{0.25}OH$ MXene with and without a compressive strain. (D) Strain-energy curve for Ti_3C_2OH and $Ti_3C_1N_1OH$.

limiting the pressure sensitivity of highly N-incorporated MXene. Our calculation results support the experimental data, confirming that $Ti_3C_{1.8}N_{0.2}T_z$ and $Ti_3C_{1.5}N_{0.5}T_z$ exhibit superior pressure-sensing performance compared to both N-free $Ti_3C_2T_x$ and N-rich $Ti_3C_1N_1T_z$.

2.5 | Real-Time Temperature Sensing Performances and Human-Machine Interface Applications of Engineered Ti-Carbonitride MXene

The fabricated MXene-based temperature sensor not only exhibits high sensitivity but also features lightweight characteristics and flexibility, allowing it to be attached to various anatomical sites to effectively detect body heat in daily applications, considering the excellent sensitivity of $Ti_3C_{1.8}N_{0.2}T_z$. Figure 4A presents the skin temperature measurements obtained from different body regions. The temperatures of the toe, leg, palm, arm, and forehead measured using an infrared camera (depicted in Figure S13) were 29.2, 32.1, 32.9, 33.5, and 35.4°C, respectively, which are in close agreement with those measured using the fabricated sensor (28.8, 32.2, 32.6, 33.8, and 35.4°C, respectively in Figure 4A). This close agreement confirms the sensor's accuracy. A decreasing trend in skin temperature from the forehead to the toes was observed, which is attributed to variations in circulatory dynamics and the distance from the heart.

Additionally, the accuracy of the sensor was validated through comparison with measurements obtained from an IR camera. As demonstrated in Figure 4B, the fabricated temperature sensor successfully detects breathing patterns. In comparison to normal breathing, shallow breathing exhibits an increased respiration rate and smaller temperature variations between inhalation and exhalation. Figure 4C illustrates the sensor's response to blowing. The temperature increased similarly during both single and three consecutive blowing events, then decreased as it returned to ambient conditions. The temperature sensor was also capable of detecting touch (Figure 4D). When a finger touched the sensor, the temperature increased due to the difference between the room temperature and the finger temperature. Furthermore, the sensor precisely detected responses to one, two, and three consecutive touches.

16163028, 0, Downloaded from https://advanced.onlinelibrary.wiley.com/doi/10.1002/adfm.202530479 by Ulsan National Institute Of, Wiley Online Library on [09/04/2026]. See the Terms and Conditions (https://onlinelibrary.wiley.com/terms-and-conditions) on Wiley Online Library for rules of use; OA articles are governed by the applicable Creative Commons License

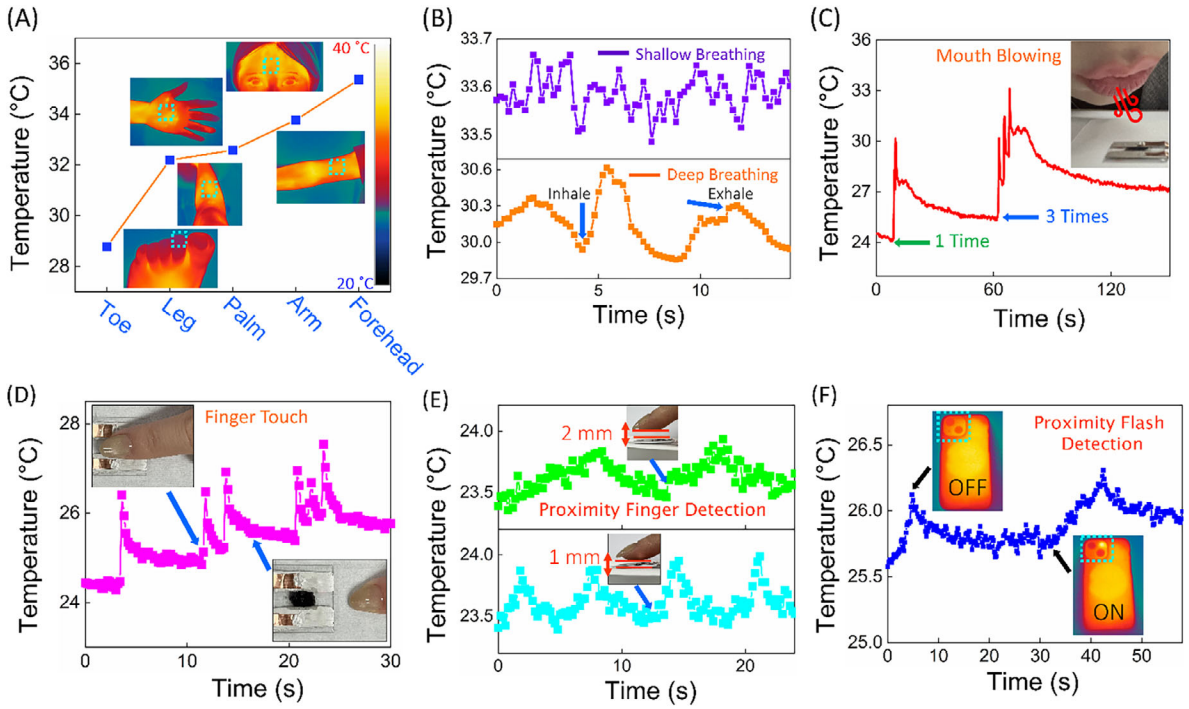

FIGURE 4 | Engineered Ti-Carbonitride MXenes-based ($Ti_3C_{1.8}N_{0.2}T_x$) temperature sensor devices' physiological and proximity/non-contact sensitivity and linearity. (A) Human skin temperature measurement at various anatomical sites, (B) Evaluation of human shallow and normal breathing patterns, (C) Blowing test with varying blowing durations, (D) Touch test for temperature-based tactile detection, (E) Proximity-based non-contact touch detection at 1 and 2 mm distances between the developed sensor and finger and (F) Detection of proximity-based flashes between the sensor and a smartphone.

The high sensitivity of the sensor enables it to detect stimuli without direct contact, solely through proximity. Figure 4E presents experimental results showing the sensor's response to a finger placed at distances of 1 and 2 mm. At 1 mm, the sensor detected a temperature change of approximately 0.5°C. Although the response speed decreased at 2 mm, the sensor still detected a temperature change of about 0.44°C. These results indicate that the sensor holds potential for applications such as contactless unlocking. In addition to proximity touch detection, the sensor was also able to detect proximity flash, as shown in Figure 4F. In this regard, we confirmed that when the flash was in the OFF state, the maximum temperature within the boxed area was 32.1°C, whereas in the ON state, the maximum temperature appeared at the flash spot and reached 33.3°C. This result indicates that the flash can sufficiently serve as a thermal stimulus. The smartphone's rear camera flash was activated and repeatedly brought near the sensor and moved away. The sensor detected subtle temperature changes each time the flash approached, confirming its ability to sense thermal variations caused by the flash. Moreover, the temperature differences caused by the flash were visualized using IR camera imaging, shown in Figure S14, further validating the sensor's functionality.

2.6 | Engineered Ti-Carbonitride MXene-based Pressure Sensor at Human-Machine Interface Applications

$Ti_3C_{1.5}N_{0.5}T_z$ Carbonitride MXene/PDMS-based pressure sensor shows high sensitivity within a wide pressure range and good flexibility. Various tests, monitoring from physiological signals to full-range human motion, were conducted to verify the sensor's feasibility in practical applications. First, the fabricated sensor, which was directly attached to the throat using medical tape, could detect the vibration of vocal cords related to speaking (red), swallowing (green), and coughing (blue) activity, as shown in Figure 5A. The more significant movements of the vocal cords and surrounding muscles result in higher current peaks, enabling the distinction of each action by simply mounting the sensor on the neck. Figure 5B shows the current changes corresponding to multiple eyes blinking when the sensor was conformally attached next to the eye. This demonstrates that the sensor can instantly detect even the minimal movements of muscles caused by blinking. The pressure sensor was mounted on the wrist to monitor the pulse beat of the radial artery, and the recorded real-time signal curve is shown in Figure 5C. From the signal, the pulse rate was calculated to be about 59 beats per minute, which closely matches the normal heart rate of a female in a relaxed condition.

In addition, the magnified view of the pulse wave in the inset graph clearly shows distinguishable percussion wave (P), tidal wave (T), and diastolic wave (D) forms, demonstrating its potential for the prediction and diagnosis of cardiovascular diseases [43, 44]. Moreover, Figure 5D shows the current signals from both sensors located in the philtrum and abdomen in response to repeated abdominal breathing. The abdomen expands during inhalation and exhalation, emits breathing air through the nose, and both locations alternately detect current peaks. Monitoring respiratory patterns enables early identification of abnormalities associated with pulmonary fibrosis and other

16163028, 0, Downloaded from https://advanced.onlinelibrary.wiley.com/doi/10.1002/adfm.202530479 by Ulsan National Institute Of, Wiley Online Library on [09/04/2026]. See the Terms and Conditions (https://onlinelibrary.wiley.com/terms-and-conditions) on Wiley Online Library for rules of use; OA articles are governed by the applicable Creative Commons License

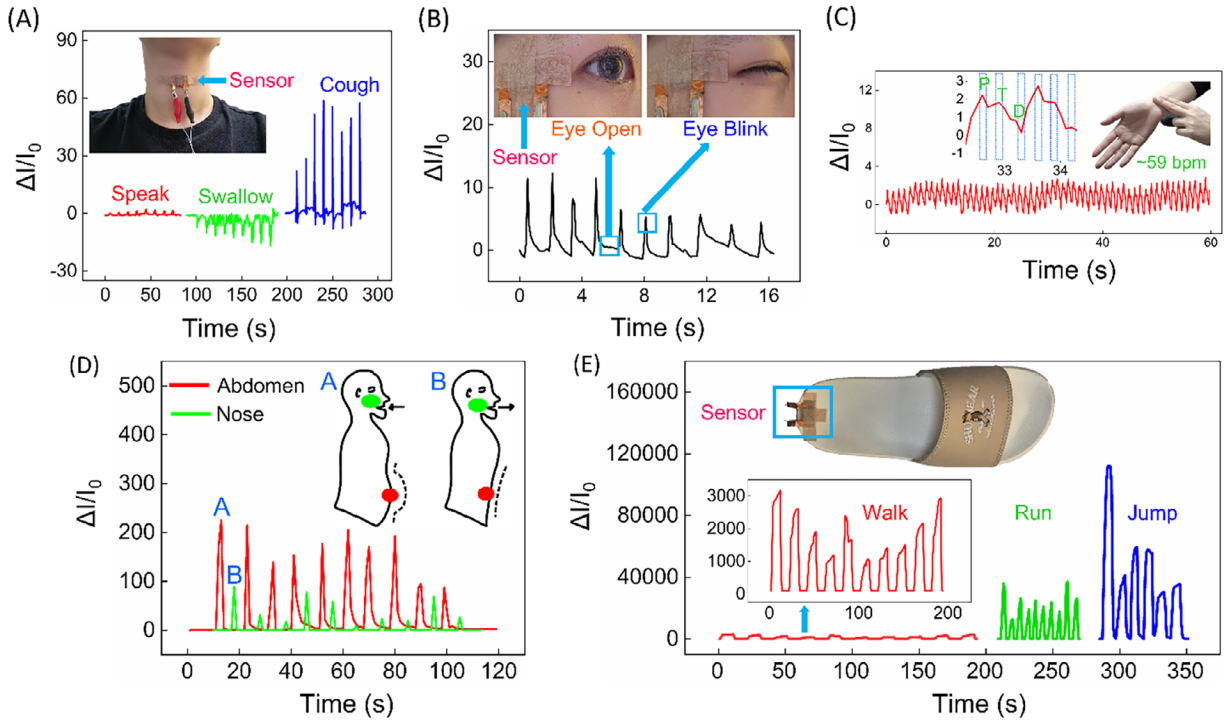

FIGURE 5 | Engineered carbonitride MXene ($Ti_3C_{1.5}N_{0.5}T_z$) real-time pressure sensor in practical monitoring of vital human motions and range of physiological activities. (A) Variation of the sensor output signal response with speaking, swallowing, coughing, (B) The signal responses during eye blinking, (C) Wrist pulse signal from the pressure sensor measuring the human radial artery, (D) Current signal at the nose and abdomen during breathing, and (E) Current signal change at the shoe's heel area during walking, running, and jumping.

cardiopulmonary diseases, and integrating such sensing functions into bionic, artificial-nervous-system architectures provides a pathway toward neuromorphic hardware capable of real-time, low-power physiological detection [45–48]. As illustrated in Figure 5E, the sensor attached to shoes at the position of the heel exhibits a fast and stable response according to gait type: walking (red), running (green), and jumping (blue). The sensor maintained consistent performance despite several impact times, demonstrating its durability and robustness in harsh conditions. Therefore, the flexible $Ti_3C_{1.5}N_{0.5}T_z$ MXene/PDMS-based pressure sensor can be easily mounted on the human skin and accurately detect physiological signals and physical activity, suggesting promising candidates for next-generation healthcare devices.

3 | Conclusions

In summary, we have successfully controlled and engineered nitrogen atoms into the Ti-Carbonitride MXene structure, resulting in high electrical conductivity (~22,727 S/cm), crystal quality, and purity. The dual multi-sensing and multitasking durable sensing performance is possible due to the precise control of nitrogen atoms in the X layers of Ti_3CNT_z (Ti-Carbonitride MXene). Nitrogen-deficient Ti-Carbonitride MXene compositional stoichiometry of $Ti_3C_{1.8}N_{0.2}T_z$ delivers an outstanding thermographic sensitivity of 15.9% $°C^{-1}$, which is ~300% higher than that of nitrogen-sufficient Ti-Carbonitride. The flexible pressure sensor also exhibited very high sensitivity and device durability, over 400% higher than those of nitrogen-sufficient Ti-Carbonitride stochiometry (Ti_3CNT_z), attributed to a delicate balance between titanium-nitrogen bonding hybridization, which requires a wider interlayer distance and facilitates the interlayer atomic movements in $Ti_3C_{1.8}N_{0.2}T_z$. Synchrotron radiation-based advanced XAFS on XANES, EXAFS, WT-EXAFS, and FT-EXAFS confirms the presence and the mechanistic role of atomic nitrogens within the well-aligned 2D-layered Ti-Carbonitride structure. Ti-Carbonitride thermographic temperature sensors detected various changes in human physiological indicators, including skin temperature, blood flow, respiration, body movement, non-contact proximity sensing, non-invasive vital human signs, motion, and healthcare monitoring electronic devices. The experimental results are in line with the general pattern observed in our DFT calculations. The enhanced temperature sensitivity in $Ti_3C_{1.8}N_{0.2}T_z$ is attributed to the boost in electrical conductivity due to N incorporation, which increases the electron density of the Ti-Carbonitride MXene. Additionally, N incorporation modulates the vibrational spectrum and lattice deformability, leading to remarkable pressure sensitivities in $Ti_3C_{1.8}N_{0.2}T_z$ and $Ti_3C_{1.5}N_{0.5}T_z$. Our findings reveal a new physicochemical phenomenon in Ti_3CNT_z MXene by incorporating controlled nitrogen atoms. This presents significant potential for customizing its optoelectronic properties and applications in a reliable and scalable sensor device fabrication for next-generation bioelectronic systems.

Acknowledgements

This work was supported by the Nano Material Technology Development Program (Grant No. RS-2024-00408180, 2021M3H4A3A02099209) through the National Research Foundation (NRF) of Korea, funded by

16163028, 0, Downloaded from https://advanced.onlinelibrary.wiley.com/doi/10.1002/adfm.202530479 by Ulsan National Institute Of, Wiley Online Library on [09/04/2026]. See the Terms and Conditions (https://onlinelibrary.wiley.com/terms-and-conditions) on Wiley Online Library for rules of use; OA articles are governed by the applicable Creative Commons License

the Ministry of Science, ICT, and Future Planning. This work was also supported by the InnoCORE program of the Ministry of Science and ICT (1.260007.01).

Conflicts of Interest

The authors declare no conflict of interest.

Data Availability Statement

The data that support the findings of this study are available from the corresponding author upon reasonable request.

References

1. S. K. Bhardwaj, H. Singh, M. Khatri, K. H. Kim, and N. Bhardwaj, "Advances in MXenes-Based Optical Biosensors: A Review," *Biosensors and Bioelectronics* 202 (2022): 113995, https://doi.org/10.1016/j.bios.2022.113995.

2. E. Singh and H. S. Nalwa, *Nanomaterial-Based Flexible and Multifunctional Sensors*, American Scientific Publishers, Los Angeles (2019).

3. D. Mohapatra, Y. Shin, M. Z. Ansari, et al., "Process Controlled Ruthenium on 2D Engineered V-MXene via Atomic Layer Deposition for Human Healthcare Monitoring," *Advanced Science* 10 (2023): 2206355, https://doi.org/10.1002/advs.202206355.

4. E. Singh, M. Meyyappan, and H. S. Nalwa, "Flexible Graphene-Based Wearable Gas and Chemical Sensors," *ACS Applied Materials Interfaces* 40 (2017): 34544–34586.

5. D. Mohapatra, J. E. Byun, M. Z. Ansari, et al., "Layer Engineered MXene Empowered Wearable Pressure Sensors for Non-Invasive Vital Human-Machine Interfacing Healthcare Monitoring," *Advanced Materials Technology* 8, no. 24 (2023): 2301175, https://doi.org/10.1002/admt.202301175.

6. J. C. Yang, J. Mun, S. Y. Kwon, S. Park, Z. Bao, and S. Park, "Electronic Skin: Recent Progress and Future Prospects for Skin-Attachable Devices for Health Monitoring, Robotics, and Prosthetics," *Advanced Materials* 31, no. 48 (2019): 1904765, https://doi.org/10.1002/adma.201904765.

7. K. S. Novoselov, D. Jiang, F. Schedin, et al., "Two-Dimensional Atomic Crystals," *Proceeding Natural Academy Science, U S A* 102, no. 30 (2005): 10451–10453.

8. M. Chhowalla, Z. Liu, and H. Zhang, "Two-Dimensional Transition Metal Dichalcogenide (TMD) Nanosheets," *Chemical Society Review* 44 (2015): 2584–2586, https://doi.org/10.1039/C5CS90037A.

9. M. Naguib, V. N. Mochalin, M. W. Barsoum, and Y. Gogotsi, "25th Anniversary Article: MXene: A New Family of Two-Dimensional Materials," *Advanced Materials* 26, no. 7 (2013): 992–1005, https://doi.org/10.1002/adma.201304138.

10. B. Anasori, M. R. Lukatskaya, and Y. Gogotsi, "2D Metal Carbides and Nitrides (MXenes) for Energy Storage," *Nature Reviews Materials* 2 (2017): 16098, https://doi.org/10.1038/natrevmats.2016.98.

11. D. Mohapatra, H. J. Kang, S. Lee, et al., "Ultrahigh Sensitivity for Thermographic Human-Machine Interface via Precious Metals Atomic Layer Deposition on V-MXene: Computational and Experimental Exploration," *Small* 20, no. 35 (2024): 2402003, https://doi.org/10.1002/small.202402003.

12. B. Anasori, Y. Xie, M. Beidaghi, et al., "Two-Dimensional, Ordered, Double Transition Metals Carbides (MXenes)," *ACS Nano* 9, no. 10 (2015): 9507–9516, https://doi.org/10.1021/acsnano.5b03591.

13. W. Guo, Z. She, H. Xue, and X. Zhang, "Density Functional Theory Study on the Ti_3CN and Ti_3CNT_2 (T = O, S and F) as High Capacity Anode Material for Na Ion Batteries," *Applied Surface Science* 529 (2020): 147180, https://doi.org/10.1016/j.apsusc.2020.147180.

14. R. Shein and A. L. Ivanovskii, "Graphene-Like Titanium Carbides and Nitrides Tin+1Cn, Tin+1Nn (n = 1, 2, and 3) from De-Intercalated MAX Phases: First-Principles Probing of Their Structural, Electronic Properties and Relative Stability," *Computational Materials Science* 65 (2012): 104–114, https://doi.org/10.1016/j.commatsci.2012.07.011.

15. G. V. Lier, C. V. Alsenoy, V. V. Doren, and P. Geerlings, "Ab Initio Study of the Elastic Properties of Single-walled Carbon Nanotubes and Graphene," *Chemical Physics Letters* 326, no. 1-2 (2000): 181–185.

16. C. E. Shuck, M. Han, K. Maleski, et al., "Effect of Ti_3AlC_2 MAX Phase on Structure and Properties of Resultant $Ti_3C_2T_x$ MXene," *ACS Applied Nano Materials* 2 (2019): 3368–3376, https://doi.org/10.1021/acsanm.9b00286.

17. E. Quain, T. S. Mathis, M. Kurra, et al., "Direct Writing of Additive-Free MXene-in-Water Ink for Electronics and Energy Storage," *Advanced Materials Technology* 4, no. 1 (2018): 1800256, https://doi.org/10.1002/admt.201800256.

18. W. Yang, J. Yang, J. J. Byun, et al., "3D Printing of Freestanding MXene Architectures for Current-Collector-Free Supercapacitors," *Advanced Materials* 31, no. 37 (2019): 1902725, https://doi.org/10.1002/adma.201902725.

19. W. Zhang, C. Cheng, P. Fang, et al., "The Role of Terminations and Coordination Atoms on the Pseudocapacitance of Titanium Carbonitride Monolayers," *Physical Chemistry Chemical Physics* 18 (2016): 4376–4384, https://doi.org/10.1039/c5cp06986f.

20. W. Jindata, K. Hantanasirisakul, T. Eknapakul, et al., "Spectroscopic Signature of Negative Electronic Compressibility from the Ti Core-level of Titanium Carbonitride MXene," *Applied Physics Review* 8 (2021): 021401.

21. M. Anayee, M. Shekhirev, R. J. Wang, and Y. Gogotsi, "Effect of Oxygen Substitution and Oxycarbide Formation on Oxidation of Ti_3AlC_2 MAX Phase," *Journal of American Ceramic Society* 107 (2024): 6334–6341, https://doi.org/10.1111/jace.19861.

22. H. K. Iqbal, J.-M. Oh, J. Chae, et al., "Effect of Substitutional Oxygen on Properties of $Ti_3C_2T_x$ MXene Produced Using Recycled TiO_2 Source," *Small Methods* 7 (2023): 2201715, https://doi.org/10.1002/smtd.202201715.

23. T. Zhang, C. E. Shuck, K. Shevchuk, M. Anayee, and Y. Gogotsi, "Synthesis of Three Families of Titanium Carbonitride MXenes," *Journal of American Ceramic Society* 145, no. 41 (2023): 22374–22383, https://doi.org/10.1021/jacs.3c04712.

24. J. Zhang, N. Kong, S. Uzun, et al., "Scalable Manufacturing of Free-Standing, Strong Ti3C2Tx MXene Films with Outstanding Conductivity," *Advanced Materials* 32 (2020): 2001093, https://doi.org/10.1002/adma.202001093.

25. J.-H. Han, J. Park, M. Kim, et al., "Ultrahigh Conductive MXene Films for Broadband Electromagnetic Interference Shielding," *Advanced Materials* 37, no. 18 (2025): 2502443, https://doi.org/10.1002/adma.202502443.

26. M. Y. Han, B. Ozyilmaz, Y. Zhang, and P. Kim, "Energy Band-gap Engineering of Graphene Nanoribbons," *Physical Review Letters* 98, no. 20 (2007): 206805, https://doi.org/10.1103/PhysRevLett.98.206805.

27. A. N. Enyashin and A. L. Ivanovskii, "Two-dimensional Titanium Carbonitrides and Their Hydroxylated Derivatives: Structural, Electronic Properties and Stability of MXenes Ti3C2 - xNx(OH)2 from DFTB Calculations," *Journal of Solid State Chemistry* 207 (2013): 42–48, https://doi.org/10.1016/j.jssc.2013.09.010.

28. K. Huang, Z. Li, J. Lin, G. Han, and P. Huang, "Two-dimensional Transition Metal Carbides and Nitrides (MXenes) for Biomedical Applications," *Chemical Society Review* 47, no. 14 (2018): 5109–5124, https://doi.org/10.1039/c7cs00838d.

29. J. Jang, J. Kim, J. Kim, et al., "Reduced Dopant-induced Scattering in Remote Charge-transfer-doped MoS2 Field-effect Transistors," *Science Advanced* 8, no. 38 (2022), https://doi.org/10.1126/sciadv.abn3181.

30. W. Lu, B. Mustafa, Z. Wang, F. Lian, and G. Yu, "PDMS-Encapsulated MXene@Polyester Fabric Strain Sensor for Multifunctional Sensing Applications," *Nanomaterials* 12, no. 5 (2022): 871, https://doi.org/10.3390/nano12050871.

31. R. Qin, X. Li, M. Hu, G. Shan, R. Seeram, and M. Yin, "Preparation of High-performance MXene/PVA-based Flexible Pressure Sensors with

16163028, 0, Downloaded from https://advanced.onlinelibrary.wiley.com/doi/10.1002/adfm.202509479 by Ulsan National Institute Of, Wiley Online Library on [09/04/2026]. See the Terms and Conditions (https://onlinelibrary.wiley.com/terms-and-conditions) on Wiley Online Library for rules of use; OA articles are governed by the applicable Creative Commons License

Adjustable Sensitivity and Sensing Range," *Sensors and Actuators: A Physical* 338 (2022): 113458, https://doi.org/10.1016/j.sna.2022.113458.

32. M. Amjadi, A. Pichitpajongkit, S. Lee, S. Ryu, and I. Park, "Highly Stretchable and Sensitive Strain Sensor Based on Silver Nanowire-elastomer Nanocomposite," *ACS Nano* 8, no. 5 (2014): 5154–5163, https://doi.org/10.1021/nn501204t.

33. N. Hu, Y. Karube, C. Yan, Z. Masuda, and H. Fukunaga, "Tunneling Effect in a Polymer/Carbon Nanotube Nanocomposite Strain Sensor," *Acta Materials* 56, no. 13 (2008): 2929–2936, https://doi.org/10.1016/j.actamat.2008.02.030.

34. Y. Ma, N. Liu, L. Li, et al., "A Highly Flexible and Sensitive Piezoresistive Sensor Based on MXene with Greatly Changed Interlayer Distances," *Nature Communications* 8, no. 1 (2017): 1207, https://doi.org/10.1038/s41467-017-01136-9.

35. S. Gong, W. Schwalb, Y. Wang, et al., "A Wearable and Highly Sensitive Pressure Sensor with Ultrathin Gold Nanowires," *Nature Communications* 5 (2014): 3132, https://doi.org/10.1038/ncomms4132.

36. M. Flygare and K. Svensson, "Influence of Crystallinity on the Electrical Conductivity of Individual Carbon Nanotubes," *Carbon Trends* 5 (2021): 100125, https://doi.org/10.1016/j.cartre.2021.100125.

37. Q. M. Al-Bataineh, A. A. Ahmad, A. B. Migdadi, and A. D. Telfah, "Effect of Ionic-Electronic Coupling on the Percolation Phenomenon of Polymer/Reduced Graphene Oxide Nanocomposite Films," *Polymer Advanced Technology* 35, no. 12 (2024): 70024, https://doi.org/10.1002/pat.70024.

38. W. S. Bao, S. A. Meguid, G. Z. H. Zhu, and G. J. Weng, "Tunneling Resistance and Its Effect on the Electrical Conductivity of Carbon Nanotube Nanocomposites," *Journal of Applied Physics* 111, no. 9 (2012): 093726, https://doi.org/10.1063/1.4716010.

39. H. Men, B. Huang, and J. Li, "Effect of Interfacial Modification on the Low-Temperature Fatigue Properties of Polymer/MXene Flexible Pressure Sensors," *ACS Applied Material Interfaces* 16, no. 6 (2024): 7489–7499, https://doi.org/10.1021/acsami.3c15243.

40. K. Krishnaswamy, B. Himmetoglu, Y. Kang, A. Janotti, and C. G. V. de Walle, "First-principles Analysis of Electron Transport in BaSnO3," *Physics Review B* 95 (2017): 205202, https://doi.org/10.1103/PhysRevB.95.205202.

41. A. Giri, J. T. Gaskins, L. Li, Y. Wang, O. V. Prezhdo, and P. E. Hopkins, "First-principles Determination of the Ultrahigh Electrical and Thermal Conductivity in Free-electron Metals via Pressure Tuning the Electron-phonon Coupling Factor," *Physics Review B* 99 (2019): 165139.

42. H. Zhu, N. Qiu, G. Fang, and S. Du, "First-Principles Study on the Structure and Electronic Properties of M2CSx (M = Sc, Ti, Y, Zr and Hf, x = 1,2," *RSC Advances* 13 (2013): 21690, https://doi.org/10.1039/d3ra03340f.

43. B. Chen, L. Zhang, H. Li, X. Lai, and X. Zeng, "Skin-inspired Flexible and High Performance MXene@Polydimethylsiloxane Piezoresistive Pressure Sensor for human Motion Detection," *Journal of Colloid Interface Science* 617 (2022): 478–488, https://doi.org/10.1016/j.jcis.2022.03.013.

44. Y. Zheng, R. Yin, Y. Zhao, et al., "Conductive MXene/Cotton Fabric Based Pressure Sensor with both High Sensitivity and Wide Sensing Range for human Motion Detection and E-skin," *Chemical Engineering Journal* 420 (2021): 127720, https://doi.org/10.1016/j.cej.2020.127720.

45. L. Yang, H. Wang, W. Yuan, et al., "Wearable Pressure Sensors Based on MXene/Tissue Papers for Wireless Human Health Monitoring," *ACS Applied Materials Interfaces* 13, no. 50 (2021): 60531–60543, https://doi.org/10.1021/acsami.1c22001.

46. X. Qin, B. Zhong, S. Lv, et al., "A Zero-Voltage-Writing Artificial Nervous System Based on Biosensor Integrated on Ferroelectric Tunnel Junction," *Advanced Materials* 36, no. 32 (2024): 2404026, https://doi.org/10.1002/adma.202404026.

47. L. Li, H. Xu, Z. Li, B. Zhong, Z. Lou, and L. Wang, "3D Heterogeneous Sensing System for Multimode Parallel Signal No-Spatiotemporal Misalignment Recognition," *Advanced Materials* 37, no. 6 (2025): 2414054, https://doi.org/10.1002/adma.202414054.

48. X. Qin, B. Zhong, H. Xu, et al., "Manufacturing High-Performance Flexible Sensors via Advanced Patterning Techniques," *International Journal of Extreme Manufacturing* 7, no. 3 (2025): 032003, https://doi.org/10.1088/2631-7990/ada857.

Supporting Information

Additional supporting information can be found online in the Supporting Information section.

Supporting File: adfm75193-sup-0001-SuppMat.docx.

16163028, 0, Downloaded from https://advanced.onlinelibrary.wiley.com/doi/10.1002/adfm.202530479 by Ulsan National Institute Of, Wiley Online Library on [09/04/2026]. See the Terms and Conditions (https://onlinelibrary.wiley.com/terms-and-conditions) on Wiley Online Library for rules of use; OA articles are governed by the applicable Creative Commons License